Triggering Anionic Redox Activity in Li 3 NbS 4 Through Cationic Disordering or Substitution

Thomas Marchandier, Sathiya Mariyappan, Maria Kirsanova, Artem Abakumov, Gwenaëlle Rousse, Dominique Foix, Moulay-tahar Sougrati, Marie Liesse Doublet, Jean-marie Tarascon

Triggering anionic redox activity in Li_3NbS_4 through cationic disordering or substitution

Thomas Marchandier,[1,2,3] Sathiya Mariyappan,[1,2] Maria A. Kirsanova,[4] Artem M. Abakumov,[4] Gwenaëlle Rousse,[1,2,3] Dominique Foix, [2,5], Moulay-Tahar Sougrati,[2,6] Marie Liesse Doublet[2,6] and Jean-Marie Tarascon[1,2,3]

1. Collège de France, Chaire de Chimie du Solide et de l'Energie, UMR 8260, 11 place Marcelin Berthelot, 75231 Paris Cedex 05, France

2. Réseau sur le Stockage Electrochimique de l'Energie (RS2E), FR CNRS 3459, 75005 Paris, France

3. Sorbonne Université− 4 place Jussieu, F-75005 Paris, France

4. Center for Energy Science and Technology, Skolkovo Institute of Science and Technology, 3 Nobel Street, Moscow, 121205, Russia

5. IPREM, CNRS, Université de Pau & Pays Adour, E2S-UPPA, Hélioparc, 2 Avenue P.Angot, 64053 Pau Cedex 9, France

6. ICGM, Univ Montpellier, CNRS, ENSCM, Montpellier, France

Abstract:

Extensive utilization of Li-ion batteries for varieties of applications necessitates ceaseless improvement of electrode materials for achieving higher energy density. Towards this goal, Li-rich layered oxides exhibiting high capacity due to cumulated cationic and anionic redox activities are under study for nearly a decade. Still, several unanswered questions remain with respect to these Li-driven anionic redox reactions in terms of the activation process and long-term consequences upon cycling. Here, we focus on the Li-rich Li_3NbS_4 phase, synthesized as two different ordered and disordered polymorphs. From an analysis of their chemical/ electrochemical properties, we unraveled a crystal-electronic structure relationship that triggers the anionic redox activity in these compounds. Moreover, through complementary theoretical calculations, we showed the capability of cationic disorder to trigger anionic redox activity via the hybridization of the cationic and non-bonding anionic energy levels. This finding was further supported by the appearance of anionic redox activity by introducing disorder through cationic substitution. Altogether, the insights derived could help in designing new anionic redox materials with optimum performances for practical applications.

Introduction:

The development of renewable energies is one of the most important challenges for our society to partially cope with global warming. The Li-ion battery technology is now firmly established in portable electronics and electric transport and is becoming a serious contender for grid applications.[1] However, the ever-increasing demand for energy density requires the improvement of these devices, in particular via the development of new high-capacity electrode materials. These constraints have naturally led to the synthesis of lithium-rich materials, including the famous Li-rich NMC with promising theoretical capacities greater than 300 $mAh.g^{-1}$.[2] However, these performances rely on the use of anionic redox activity which is far more complex than the cationic one, and lead to a few roadblocks in terms of applications (i.e poor energy efficiency, voltage fade).[3] Indeed, in spite of numerous experimental and theoretical works, many questions remain about this process and in particular concerning its activation.

Thus, while it is now well established that the anionic redox activity in Li-rich compounds is conditioned to the presence of non-bonding electron pairs on the anions,[4] the mechanism of their activation is far to be fully elucidated. For instance, the so-called "d^0 compounds" such as Li_2ZrO_3, Li_2TiO_3 or Li_2TiS_3 are *a priori* ideal candidates for studying anionic redox processes because they possess non-bonding electronic doublets on their anions and their *nd* transition metal bands are empty, preventing any cationic redox. Yet, these compounds are systematically and mysteriously electrochemically inactive. Intrigued by these observations, many research groups have shown that it was possible to activate these phases by making cationic substitutions ($Li_2Ru_yTi_{1-y}O_3$,[5] $Li_2Fe_yTi_{1-y}S_3$[6] etc…). From these results, it has been suggested that the activation of anionic redox was related to the hybridization of the non-bonding doublet of the anions with the electronic states of transition metals,[7] without however, bringing a complete scientifically sound general framework to account for this problem.

At this point, Li-rich sulfide Li_3NbS_4 attracted our attention as it consists of d^0 Nb^{5+} but it was reported to exhibit anionic redox activity when prepared by mechanosynthesis.[8,9] Li_3NbS_4 crystallizes in a disordered rock-salt structure in contrast to a layered rocksalt structure of Li_2TiO_3, Li_2TiS_3 etc. In this case, the legitimate question is if the structure plays a role in activating the anionic redox? If so, how? With this idea in mind, we revisit the synthesis of Li_3NbS_4 and managed to synthesize it with two different structures: a high temperature polymorph with the ordered structure (o-Li_3NbS_4) and a disordered rocksalt polymorph (d-Li_3NbS_4) synthesized by high energy ball-milling. Using these two polymorphs of Li_3NbS_4 and combining electrochemical and structural analyses by X-ray diffraction and electron microscopy, we demonstrate that the observed difference in the electrochemical behavior of

the polymorphs is the direct consequence of the cationic order/disorder. Further analysis by XPS shows that this structure-related activation is a consequence of the anionic nature of the oxidation process. In addition, we completed our study by exploring several cationic substitutions (Fe^{2+}, Mn^{2+}, etc) on Li_3NbS_4. Finally we rationalized all these results with the help of theoretical modeling and propose a general framework to explain the rules for triggering anionic redox. Beyond the fundamental approach, we hope that this study will inspire chemists to synthetize anionic-redox active compounds without compromising their high capacity.

Experimental:

Synthesis: The synthesis of d-Li_3NbS_4 was performed following a previously reported protocol.[9] About 500 mg of d-Li_3NbS_4 was synthesized by mixing in an Ar-filled glovebox, niobium powder (Alfa-Aesar, 99.99 %), lithium sulfide (Alfa-Aesar, 99.9 %) and elemental sulfur (Sigma-Aldrich, 99.998 %) using a 10% excess of Li_2S over the stoichiometry. The powder was then transferred into a 45 mL zirconia jar with 11 zirconia balls (10 mm diameter, 2.4 gram weight) and ball milled using a Pulverisette 7 instrument at 550 rpm for 60 hrs. After the reaction, the jar was opened in an Ar-filled glovebox and the powder was collected. For o-Li_3NbS_4 the same procedure was followed to get the precursor mixture, but instead of transferring the reagents into a ball mill jar the homogeneously hand grinded mixture was transferred into a carbon coated quartz ampoule and subsequently sealed under dynamic vacuum (~10^{-3} mbar). The resulting ampoule was then placed in an oven at 650 °C for 60 hours before being opened in a glove box under Ar atmosphere. The collected powder was then stored as such. The syntheses of $Li_{1.2}Nb_{0.4}Fe_{0.4}S_2$ and $Li_{1.13}Nb_{0.38}Mn_{0.5}S_4$ were performed using niobium powder, lithium sulfide, iron sulfide/ manganese sulfide (Alfa-Aesar, 99.9 %) and elemental sulfur in stoichiometric amounts following the same procedure as for o-Li_3NbS_4.

X-ray diffraction: Synchrotron X-ray powder diffraction (SXRD) patterns were measured either in the MSPD beamline of the ALBA synchrotron[10,11] (Barcelona, Spain) with λ = 0.41378 Å or at the 11-BM beamline of the Advanced Photon Source (Argonne National Laboratory) with λ = 0.45789 Å. To limit absorption, the powders were mixed with dried amorphous silica in an Ar-filled glovebox and sealed in glass capillaries of 0.6 mm diameter. Operando powder X-ray diffraction (XRD) experiments were performed in an airtight electrochemical cell equipped with a Be window, assembled in an argon filled glovebox. The patterns were then collected in Bragg−Brentano geometry using a Bruker D8 Advance diffractometer equipped with a Cu K_α X-ray source (λ_1 = 1.5406 Å, λ_2= 1.5444 Å) and a LynxEye XE detector. Finally, the refinement of the diffraction patterns was done following the Rietveld method using the FullProf program.[12]

Electrochemical measurements: Swagelok-type cells were assembled in an argon-filled glovebox using positive electrodes made by hand grinding the active materials with 20 % in mass carbon Super P and lithium metal as the negative electrode. Both electrodes were separated by a Whatmann GF/D borosilicate glass fibers sheets cut to appropriate size and soaked in LP30 electrolyte (1 M $LiPF_6$ in a mixture of EC/DMC 1:1 by volume). The cells were then cycled at C/20 rate in a Biologic galvanostat/ potentiostat (MPG-2/ VMP-3) using galvanostatic (constant current) mode.

Electron microscopy: Samples for transmission electron microscopy (TEM) were prepared in an Ar-filled glove box by grinding the powders in an agate mortar in dimethyl carbonate and depositing drops of suspension onto holey TEM grids with Lacey Formvar/Carbon support layer. The samples were transported to the TEM column by means of a Gatan vacuum transfer holder, thus completely avoiding the contact with air and moisture. Electron diffraction (ED) patterns, high resolution transmission electron microscopy (HR-TEM) images, high angle annular dark field (HAADF-) and annular bright field (ABF-) scanning transmission electron microscopy (STEM) images were collected with a probe-corrected Titan Themis Z electron microscope operated at 200 kV. Energy dispersive X-ray (EDX) maps and spectra were collected in the STEM mode with a Super-X EDX system.

X-ray photoemission spectroscopy: X-ray photoemission spectroscopy (XPS) measurements were carried out with a THERMO Escalab spectrometer, using focused monochromatic Al Kα radiation (hv = 1486.6 eV) and equipped with an argon-filled glove box allowing to preserve the samples from moisture and air at all times from their preparation to their analysis. Peaks were recorded with constant pass energy of 20 eV. The pressure in the analysis chamber was around 5×10^{-8} mbar. The binding energy scale was calibrated using the C 1s peak at 285.0 eV from the hydrocarbon contamination present at the samples surface. The spectra were fitted using a minimum number of components. Several spectra were recorded at different times to check that the samples were not subjected to degradation during the X-ray irradiation.

Mossbauer spectroscopy: Room temperature standard and *in situ* ^{57}Fe Mossbauer analyses were carried out in the transmission geometry in the constant acceleration mode and with a ^{57}Co(Rh) source with an radioactivity of 350 MBq. The velocity scale (±4 mm s^{-1}) was calibrated at room temperature with α-Fe foil. Regarding the low amount of iron in the sample $Li_{1.2}Nb_{0.4}Fe_{0.4}S_2$, 80 mg of powder were needed to get a good spectrum in 72 hours. During cycling, spectra were collected for 24 hrs at selected voltages. Self-standing electrodes were used for the study that contain 30 mg/cm² mixed with 25% of carbon black and 5% of polytetrafluoroethylene (PTFE) binder. The hyperfine parameters IS (isomer shift) and QS (quadrupole splitting) were determined by fitting Lorentzian lines to the experimental data. The complete set-up of the *in situ* cell used was described elsewhere.[13]

Results

1. Synthesis, crystal structures and electrochemical tests

The synthesis of both ordered (o-Li_3NbS_4) and disordered (d-Li_3NbS_4) polymorphs were started from the same precursor mixture of Li_2S, Nb and S in a stoichiometric ratio that was hand grinded for 10 min in an Ar-filled glove box. The d-Li_3NbS_4 polymorph was obtained by mechanosynthesis via grinding the precursor mixture in a planetary ball-mill while the o-Li_3NbS_4 polymorph was synthesized at high temperature (650°C) in a quartz ampule (see experimental section for further details). A Rietveld refinement of the X-ray powder diffraction pattern of the mechanically synthesized d-Li_3NbS_4 compound confirmed the disordered rocksalt-type cubic structure ($Fm\bar{3}m$, a = 5.1412(2) Å) described by Sakuda et al.[9] (see Figure 1 a,b and Table S1). Moreover, transmission electron microscopy images showed that the sample consists of highly agglomerated crystalline nanoparticles of 5 to 10 nm in size (see Figure S1), which is consistent with the width of the peaks observed in X-ray diffraction pattern. Finally, an EDX analysis (cf. figure S1) of the sample confirmed the expected Nb/S ratio of 4 for this compound.

Next, the o-Li_3NbS_4 polymorph, as far as we know, has never been reported and thus required more detailed crystallographic investigation. A first indexation of the synchrotron XRD (SXRD) pattern suggested an I-centered cubic lattice and electron diffraction (cf. Figure S2) confirmed the space group $I\bar{4}3m$ with a = 10.2973(2) Å. This similarity with the Li_3NbO_4 oxide[14] naturally led to the proposal of an identical structural model, later confirmed by the Rietveld refinement of the SXRD pattern (cf. Figure 1c and table S2). Structurally, o-Li_3NbS_4 shares with d-Li_3NbS_4 the same close-packed arrangement of cations and anions but differs from the disordered polymorph by a segregation of lithium and niobium crystallographic sites. Indeed, the NbS_6 octahedra in o-Li_3NbS_4 are linked to each other by the edges to form isolated Nb_4S_{16} tetramers (cf. Figure 1 d and e), whereas the lithium atoms occupy the remaining octahedral spaces (not shown). However, it is important to note that at first the refinement did not allow a decent fit of some reflections (cf. Figure S3). In order to understand the origin of this discrepancy, a complementary transmission electron microscopy study was conducted. This analysis showed the presence of disordered domains within the crystallites of the ordered phase (cf. Figure S4). However, taking into account this phenomenon in the refinement resulted only in a very low rate of disordered phase (<1%) and did not allow to improve the fit. Then, HAADF-STEM images demonstrated presence of antiphase boundaries (APBs) (cf. Figure S5) which arise when one ordered domain is shifted over $a/4$ with respect to another, closely resembling those previously observed in $Li_3Ru_{0.1}Nb_{0.9}O_4$.[15] Thus, this phenomenon was taken into account in the refinement, using selective

broadening conditions dependent of the h,k,l indexes, and lead to a significant improvement of the fit (cf. Figure S3).

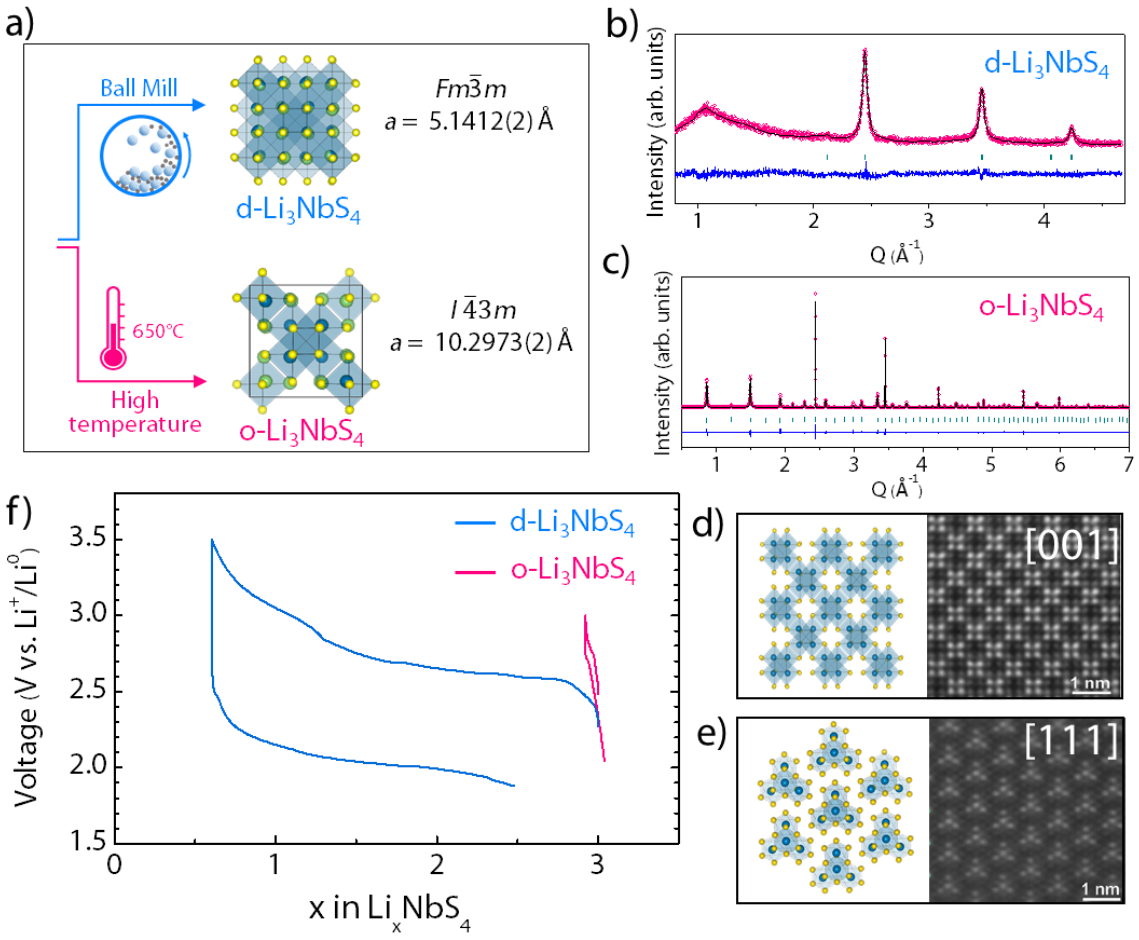

Figure 1: (a) Structures of d-Li_3NbS_4 and o-Li_3NbS_4 with the corresponding methods of synthesis in the left. (b) X-ray Rietveld refinement of d-Li_3NbS_4 (resp. o-Li_3NbS_4) at 300 K. (c) X-ray Rietveld refinement of o-Li_3NbS_4 at 300 K. The wavelength used for synchrotron X-ray is λ = 0.4137Å. For both (b) and (c) the pink circles, black continuous line, and bottom blue line represent the observed, calculated, and difference patterns, respectively. Vertical green tick bars stand for the Bragg positions. These plots can be found enlarged in the figure S3. (d) and (e) high resolution HAADF-STEM images of o-Li_3NbS_4 along [001] and [111] directions and the corresponding structure projections. (f) First cycle voltage−composition trace of d-Li_3NbS_4 (blue) and o-Li_3NbS_4 (pink) starting with oxidation and cycled at C/20.

Next, the electrochemical properties of the two Li_3NbS_4 polymorphs as cathodes for lithium batteries were studied (cf. Figure 1f). As previously reported,[9] it is possible to reversibly remove 2.5 lithium atoms from the d-Li_3NbS_4 compound on first charge in which ~2 lithium is re-inserted with an over potential of 0.65 V between charge and discharge. A reversible capacity of ~240 mAh g-1 is achieved with d-Li_3NbS_4, but the capacity decays upon repeated cycling (cf. Figure S6).

On the contrary, it is nearly impossible to remove lithium from o-Li_3NbS_4 polymorph and the compound does not present any electrochemical activity within the tested potential window of 2.0-3.0 V. In view

of this observed drastic difference in electrochemical behavior between the two polymorphs a legitimate question regards the origin of such a difference. To address this seminal question we study one by one, the different possible parameters that could have an influence on the electrochemical behavior of the materials.

2. Effect of particle size and cationic disorder on the electrochemical behavior

It is well accepted in literature that reducing the particle size can enhance electrochemical reactivity.[16] The d-Li_3NbS_4 polymorph being synthesized by high energy ball-milling exhibit nano-sized particles in contrary to the micron-sized particles in o-Li_3NbS_4. Therefore, to investigate the effect of particle size on electrochemical behavior, the d-Li_3NbS_4 compound was annealed for 12 hours at different temperatures ranging from 100°C to 450°C in vacuum inside a sealed quartz ampoule. The samples were analyzed by XRD for the crystal structure and particle size (see Figure 2a). With increasing annealing temperature, two main effects were observed. On the one hand, a progressive sharpening of the diffraction peaks is observed and, on the other hand, beyond 400°C the appearance of superstructure peaks is noted. This indicates an increase in particle size/ crystallinity of the material and a progressive ordering of the lithium and niobium atoms through heating, respectively.

The annealed samples were then studied for their electrochemical activity in Li-cells and the voltage vs composition figures are shown in Figure 2b. A clear reduction in capacity is observed with increasing annealing temperature and the material heated at 450 °C showed almost no electrochemical activity. Finally, in order to link the structural evolution with the electrochemical properties, each of the X-ray diffraction patterns were refined with the Rietveld method which allowed extracting the apparent size of the crystallites as well as the percentage of disorder of the cationic sites (according to a method detailed in the Supplementary information III). It is worth mentioning that the size of the crystallites obtained from XRD for the pristine d-Li_3NbS_4 (not sintered) is in good agreement with the one measured from TEM. Thus, using these results the evolution of the electrochemical capacity (number of lithium extracted on the first charge) of the materials together with the size of the crystallites and cationic disorder were plotted as function of annealing temperature in Figure 2c. From this, it is clear that the decrease of the reversible capacity with annealing is closely associated to the increase of the crystallite size and to the appearance of a crystallographic order between the cations. However, it is difficult to decouple these two effects.

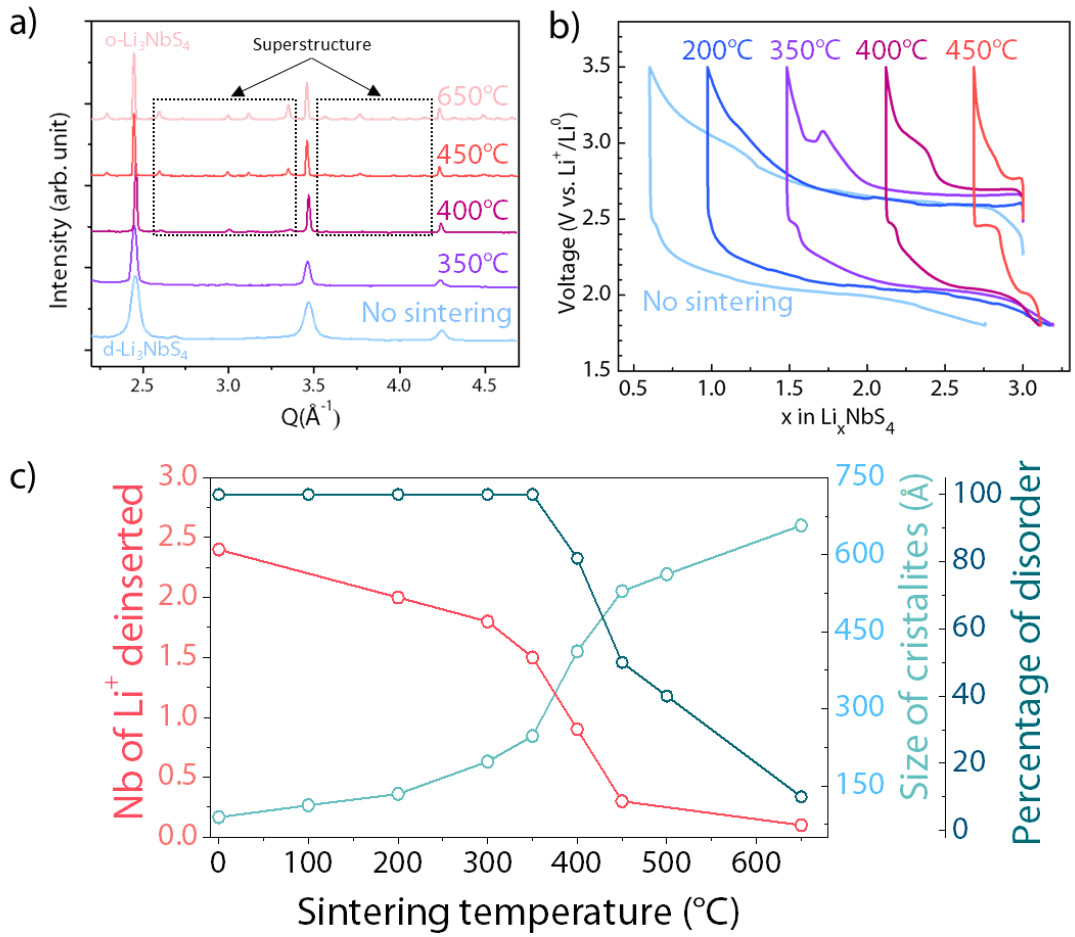

Figure 2: (a) X-ray diffraction pattern of d-Li_3NbS_4 powders annealed for 12 hours at different temperatures. The Q regions where the superstructure peaks appear are highlighted. (b) First cycle voltage–composition trace of the annealed powders. (c) Evolution of the number of lithium deinserted during the first charge, of the size of the crystals determined by Rietveld refinement and of the percentage of cation disorder as a function of the sintering temperature of d-Li_3NbS_4.

Next, we tried to understand the inactivity of o-Li_3NbS_4. Similar electrochemical inactivity was already reported for isostructural Li_3NbO_4 that was ascribed to its insulating behavior due to d^0 Nb^{5+} ions with empty 4d bands. By making the material slightly conductive with Ru^{4+} substitution, the resulting $Li_3Nb_{0.9}Ru_{0.1}O_4$ was capable of inserting lithium atoms into the structure. In order to analyze this electronic conductivity effect, since we cannot remove lithium from o-Li_3NbS_4, we tried to insert lithium into the o-Li_3NbS_4, and the cycling figure is shown in Figure 3.

3. Insertion of Lithium into o-Li_3NbS_4

From Figure 3a, it can be seen that nearly two lithium cations can be inserted into o-Li_3NbS_4 with the reduction occurring through a plateau at 1.3 V until x = 5.0 (with x the number of lithium in Li_xNbS_4).

The subsequent charge appears to operate via a different electrochemical process at 1.7 V till x = 3.2. Beyond this point a new plateau is observed around 2.6 V until x = 2.1. This last process (labelled as 4 in Figure 3a) seems to be reversible in discharge with a polarization between oxidation and reduction of 0.5 V (see Figure S7). In short, once the lithiation of Li_3NbS_4 is carried out, it activates the lithium removal on subsequent charge. To understand the origin of this phenomenon, an operando X-ray experiment has been performed (cf. Figure 3b).

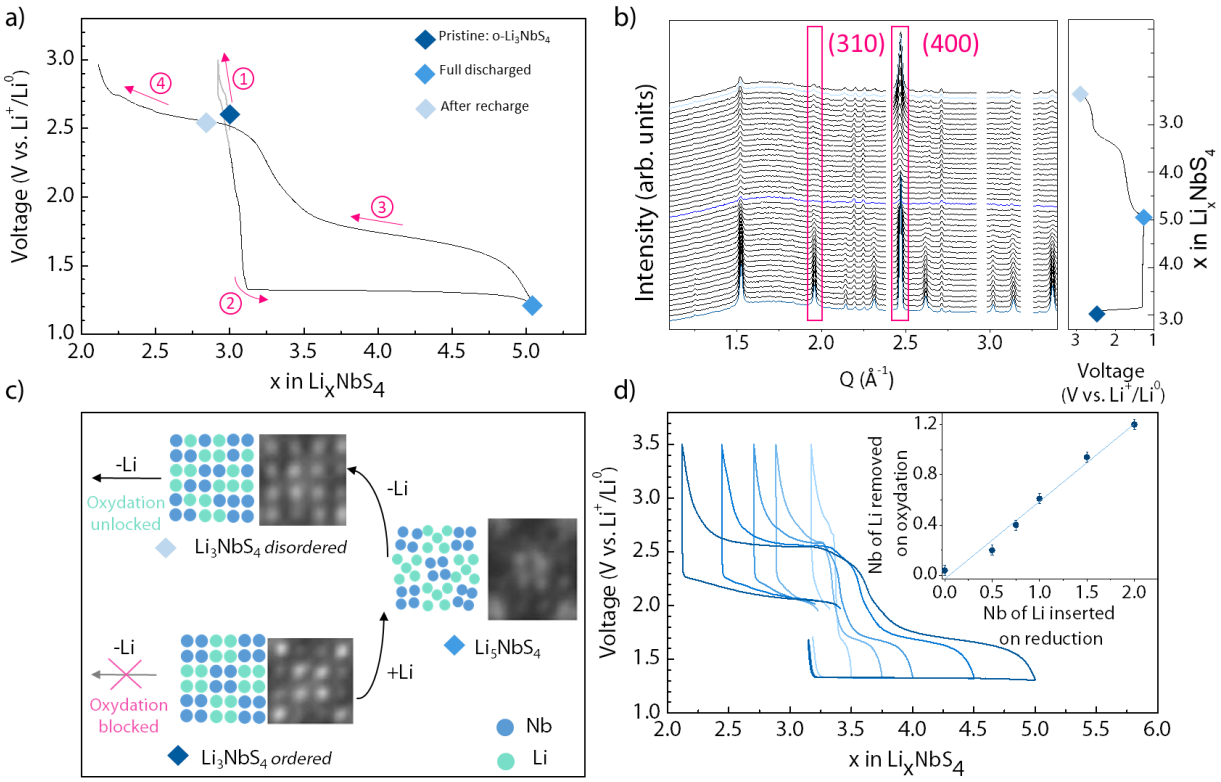

Figure 3: (a) First cycle voltage–composition trace of o-Li_3NbS_4 starting in reduction. The pink arrows indicate the direction of cycling. (b) Operando XRD patterns during the first cycle of o-Li_3NbS_4 starting with reduction with the corresponding galvanostatic curves in the right panel. The compounds are cycled at C/20 and the XRD patterns were measured for every 1 h (0.05 Li insertion/ removal). The XRD patterns corresponding to o-Li_3NbS_4, Li_5NbS_4 and r-Li_3NbS_4 (Li_3NbS_4 after discharge and re-charge) are plotted in navy, sky and light blue respectively. The (310) and (400) reflections are framed in pink color to highlight the evolution of the intensity ratio between the o-Li_3NbS_4 and the r-Li_3NbS_4. (c) Schematic of the structural evolution of Li_3NbS_4 during lithium insertion/disinsertion. HAADF-STEM images of the Nb_4S_{16} tetramers are represented for each steps of the mechanism. (d) Evolution of the voltage-composition trace of o-Li_3NbS_4 as a function of the number of lithium initially inserted. The insert represents the evolution of the number of lithium extracted by the 2.6 V electrochemical processes as a function of the number of lithium initially inserted in o-Li_3NbS_4.

A biphasic process is observed during discharge throughout the 1.3 V plateau, where the intensity of the reflections associated with the pristine material decreases in favor of an amorphous or poorly crystallized phase. In recharge, peaks reappear progressively at positions corresponding to the reflections of the pristine phase with nevertheless very different relative intensities, indicating a probable modification of the cationic order. This last hypothesis was verified by a Rietveld refinement

of the XRD pattern measured at x = 3.2, which indicated a percentage of disorder of 84% between niobium and lithium atoms. Upon further lithium removal (from x = 3.2 to x = 2.5), no remarkable changes in the XRD patterns are observed.

These results coupled with those of the previous section strongly suggest that the activation of the oxidation of the compound below x = 3 is directly related to the cationic disorder obviously generated by the prior insertion step. To clarify this, and, in particular, to better understand the structural process involved in the first oxidation plateau, a complementary TEM study was carried out.

The Li_5NbS_4 compound has been studied first. In spite of apparent absence of sharp reflections in the powder XRD pattern, its crystallites demonstrate well-defined electron diffraction patterns (cf. Figure S8). In addition, HAADF-STEM images (cf. Figure S9) indicate the co-existence of two crystalline phases: one cubic with a 10.3x10.3Å *ab* mesh that is equivalent to pristine o-Li_3NbS_4 and the other one is lithiated and distorted with the 10.3x12.3Å *ab* mesh. At crystallite level, the lithiated phase is then fragmented into small domains being interrupted with lamellas of the pristine phase of 3-5 nm in width (cf. figure S9). Structurally, the main difference between the pristine and lithiated compounds comes from the structure of the Nb_4S_{16} tetramers. Indeed, perfect positional order is maintained within the tetramers of the pristine phase, whereas random atomic displacements appear in the tetramers of the lithiated phase (cf. Figure 3c and S9). Although the tetramers appear to perfectly follow the 10.3x12.3Å lattice, the exact atomic positions within the tetramers lose long-range correlations resulting in quasi-amorphous state observed with XRD.

In a second step, TEM analysis of the compound obtained after the removal of about 2 lithium from Li_5NbS_4 (referred as recharged-Li_3NbS4 or r-Li_3NbS_4 in the following text) confirms an increase of the cationic disorder. Within the particle, this disorder is expressed in a biphasic way with an inter-growth of o-Li_3NbS_4 and d-Li_3NbS_4 (cf. figure S10). It is reasonable to think that the cationic disorder observed in this phase is a direct consequence of the atomic position disorder observed in the Li_5NbS_4 phase. Moreover, in comparison with the pristine phase, the successive lithium insertion/removal processes do not seem to have a significant effect on the particle size. Thus, these results suggest that the activation of the oxidation of o-Li_3NbS_4 comes only from the Nb/Li disorder. To highlight this, we studied the charge capacity evolution as a function of the amount of lithium inserted in o-Li_3NbS_4 (x = 3.5 , 4.0 …) (cf. figure 3d). The results in figure 3d show that the charge capacity increases with the conversion rate of o-Li_3NbS_4 to Li_5NbS_4 in a linear way. It demonstrates that the activation of Li_3NbS_4 oxidation is directly related with the amount of disordered regions created in the material. Thus, these results show unambiguously the primordial role of the cationic disorder in triggering the electrochemical activity of Li_3NbS_4 in oxidation (de-insertion of lithium).

At this stage, it remains to understand the charge compensation mechanism and how the cationic disorder helps in triggering the electrochemical activity of o-Li_3NbS_4 and d-Li_3NbS_4. To do this, we carried out XPS analyses of the o- and d-Li_3NbS_4 at different stages of oxidation and reduction.

4. Charge compensation mechanisms

XPS spectra of Nb 3d and S 2p were collected for both polymorphs at different states of charge (cf. figure S11) and the evolution of the proportion of charged species is shown in Figure 4. Starting with o-Li_3NbS_4, the analysis of the spectra indicates that the pristine material is mainly composed of Nb^{5+} and S^{2-} with traces of Nb^{4+} and oxidized sulfur referred as S^{n-} in the following text. The trace amount of Nb^{4+} and S^{n-} could be related to the surface reactivity of the material during synthesis and/or on exposure to air. By insertion of lithium (Li_4NbS_4 and then Li_5NbS_4), the Nb^{5+}/Nb^{4+} ratio decreases while the S^{2-}/S^{n-} ratio remains constant indicating a cationic reduction. However, it is interesting to note that the S2p spectra of Li_4NbS_4 and Li_5NbS_4 are marked by a significant amount of highly oxidized sulfur species. However, the quantification on the Li/Nb ratio and further analyses on the spectra indicate that such increase in oxidized sulphur is probably due to a slight conversion reaction in competition with the insertion one forming elemental sulfur or polysulfides on the surface of the particles themselves (see supplementary information for further explanations). Upon recharge, the XPS spectra of $Li_{3.5}NbS_4$ (point 4 in Figure 4a) is very similar to those of the pristine particles, with mainly S^{2-} and Nb^{5+}, indicating that the electrochemical behavior is reversible from the point of view of charge compensators. Lastly upon further oxidation (up to Li_2NbS_4) the redox process is marked by a sharp decrease of S^{2-} species to the benefit of S^{n-} ones indicating sulphur oxidation; while surprisingly the Nb^{5+}/Nb^{4+} ratio decreases significantly showing possible niobium reduction. To better understand this apparent contradictory behavior, a count of Nb and S charge evolution (considering S^- as the oxidized sulfur species) during this last oxidation step has been done indicating that the negative charge brought by Li removal and Nb reduction is well compensated by sulfur oxidation. This confirms that sulfur oxidation and niobium reduction are concomitant and refer to reductive coupling mechanism as already observed in oxides.[17] A similar charge evolution is observed with XPS spectra of d-Li_3NbS_4 upon oxidation (cf. figure S12). S 2p and Nb 3d spectra of the pristine material are found close to the ordered polymorph ones with however a S^{2-}/S^{n-} ratio slightly smaller for d-Li_3NbS_4. Upon lithium removal a sharp oxidation of S^{2-} into S^{n-} with a concomitant reduction of Nb^{5+} into Nb^{4+} is observed. On subsequent discharge the niobium redox state is found almost unchanged while the sulfur is only slightly reduced, therefore, this mechanism does not seem, at least in appearance, reversible.

Altogether, the XPS results demonstrate that lithium insertion in o-Li_3NbS_4 occurs though cationic redox while its removal in both polymorphs occurs through anionic redox with participation of the

cations via reductive coupling mechanism. Thus, the possibility to perform cationic reduction indicates that the inactivity of o-Li_3NbS_4 in oxidation is nested in the unfeasibility of the anionic redox process. In other words, the cationic disorder of the compound seems to activate the anionic redox activity.

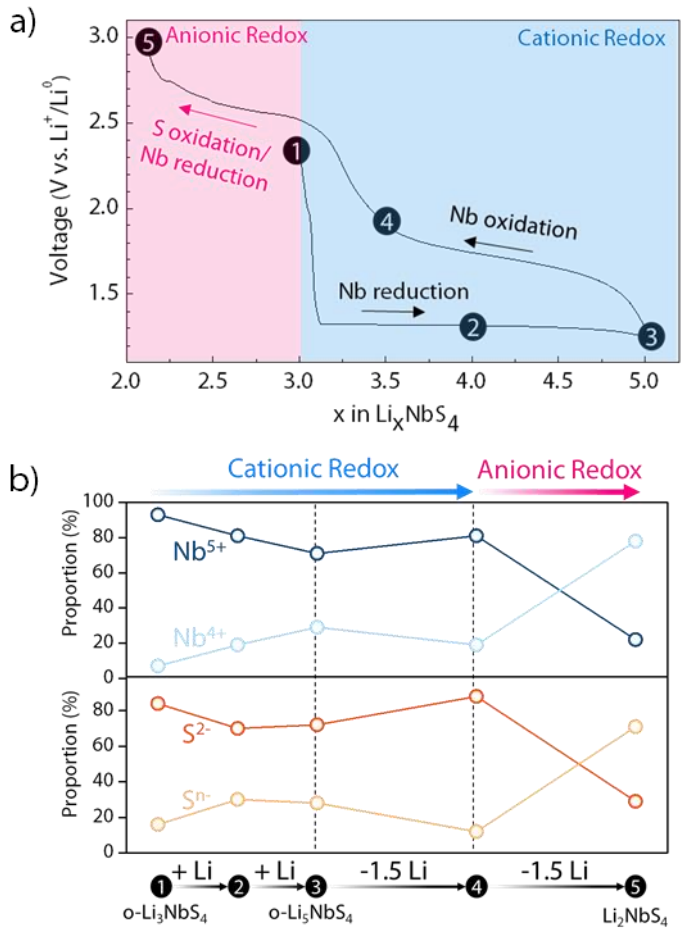

Figure 4: (a) Electrochemical cycling curve of o-Li_3NbS_4; the numbered points correspond to the ex-situ samples prepared for XPS analysis. The blue area corresponds to the mainly cationic electrochemical process, while the pink area corresponds to the anionic redox process. (b) Evolution of Nb^{5+}/Nb^{4+} and S^{2-}/S^{n-} species as deduced from XPS analysis.

At this stage, it is legitimate to wonder if anionic redox process in Li_3NbS_4 can be activated by another approach aside from disordering. An alternative, in light of previous studies dealing with Li_2MnO_3 or Li_2TiS_3, could consist in the substitution of redox inactive Ti^{4+}/ Mn^{4+} by redox active cation such as Fe^{2+} and Ti^{3+}. With this idea in mind, we embarked on synthesis exploration of substituted Li_3NbS_4 phases.

5. Cationic substitution

Different Li_3NbS_4-MS (M = V, Cr, Mn, Fe or Co) solid solutions have been investigated. Among all syntheses trials, only two compounds with a cationic mixture could be obtained in a pure form, namely $Li_{1.2}Nb_{0.4}Fe_{0.4}S_2$ (LNFS) and $Li_{1.12}Nb_{0.38}Mn_{0.5}S_2$ (LNMS). The synthesis of these two compounds were

performed using niobium powder, lithium sulfide, iron sulfide/ manganese sulfide (Alfa-Aesar, 99.9 %) and elemental sulfur in stoichiometric amounts and following the same procedure as for o-Li_3NbS_4.

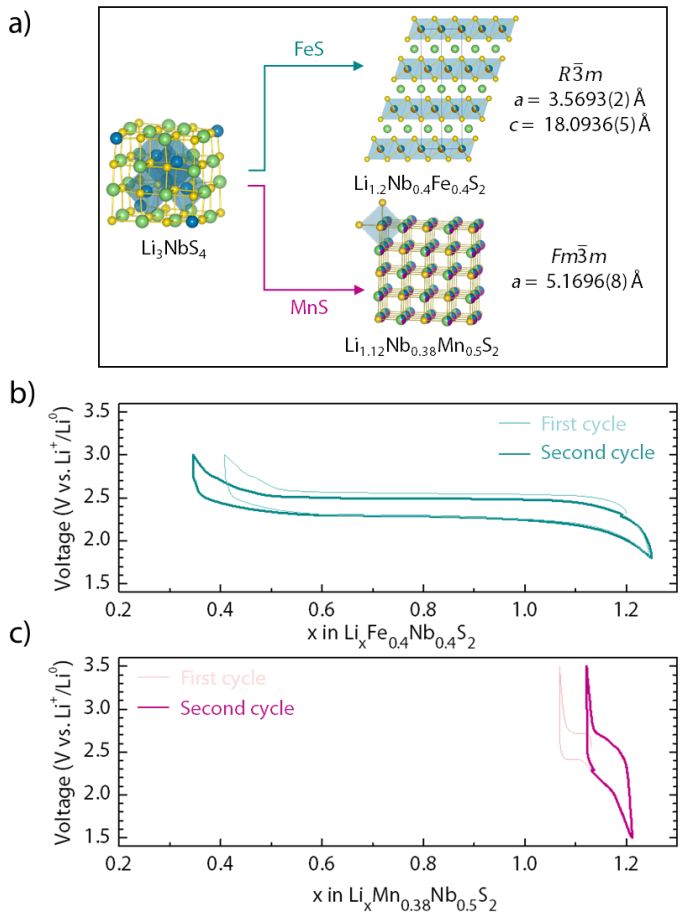

Figure 5: (a) Structures of $Li_{1.2}Nb_{0.4}Fe_{0.4}S_2$ and $Li_{1.12}Nb_{0.38}Mn_{0.5}S_2$. (b) and (c) First and second cycle voltage composition trace of LNFS (b) and LNMS (c) respectively. It is worth mentioning that the amount of reversibly inserted lithium in LNFS increases slightly cycle after cycle probably due to an electrochemical milling effect.

It is interesting to note that the two materials LNFS and LNMS have a different structure (cf. figure 5a). While the Mn-substituted material crystallizes in the form of a disordered rock salt, the iron-bearing compound adopts a layered O3-type structure similar to $Li_{1.13}Ti_{0.57}Fe_{0.3}S_2$ (LTFS).[6] This difference in structure between the two Nb-based compounds can perhaps be related to the different size of the Fe^{2+} and Mn^{2+} atoms. Fe^{2+} being closer in ionic radius to that of Nb^{5+} , but more importantly due to the fact that Mn^{2+} is a crystal-field free atom opposed to Fe^{2+}, hence being more prone to favor disordered structures.

Electrochemical cells were assembled to determine the electrochemical behavior of the substituted samples. It is possible to remove 0.9 lithium per formula unit from $Li_{1.2}Nb_{0.4}Fe_{0.4}S_2$ (LNFS) at a potential around 2.45 V in a reversible way (figure 5b) while $Li_{1.12}Nb_{0.38}Mn_{0.5}S_2$ (LNMS) is found to be mostly inactive (figure 5c). Such inactivity of the disordered rock salt phases is frequently observed with

compounds having reduced Li/transition metal ratio (poor Li content) and explained to be associated with the limited lithium percolation pathway for the Li-removal as already deeply discussed in literature[18]. Here the composition is particularly poor in lithium and the particles formed at high temperature are much larger than those obtained by mechanical synthesis. The combination of these two effects probably explains the lack of activity of this compound.

Due to the electrochemical inactivity of the Mn-substituted Li_3NbS_4, we continued further analyses solely on LNFS. The operando XRD analysis of LNFS (cf. figure S13), showed a biphasic process upon charge which is reversible on discharge. The XRD pattern of the delithiated LNFS is difficult to interpret and solely the growth of a peak at lower angle than the (003) of the pristine is observed. Next, we studied the oxidation state of the iron and sulfur in the compound during cycling by in-situ Mössbauer spectroscopy and XPS (cf. figure 6).

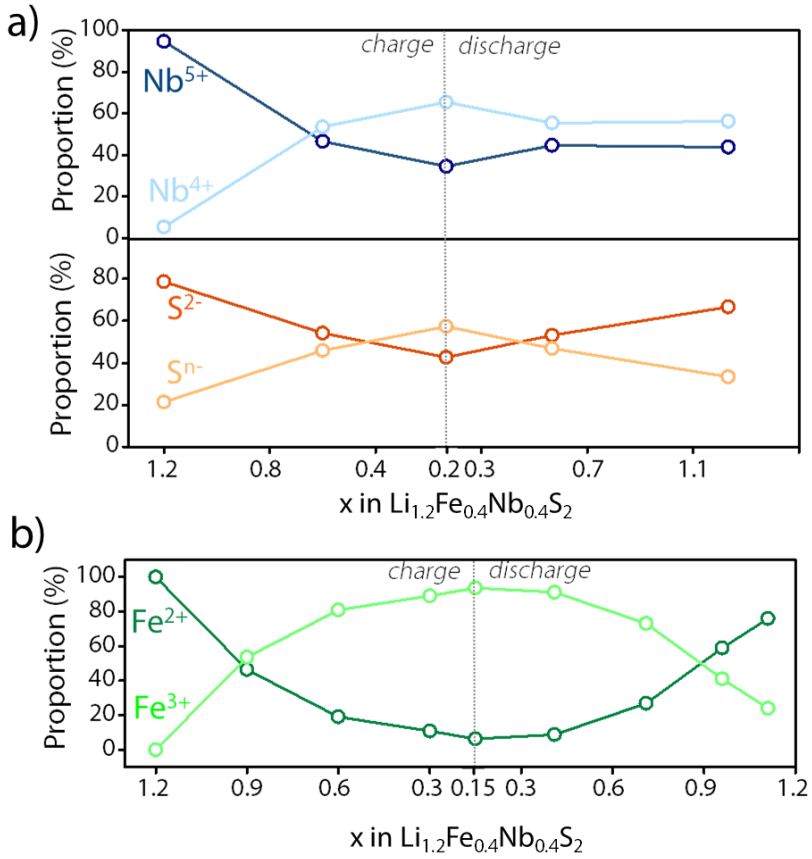

Figure 6: (a) Evolution of Nb^{5+}/Nb^{4+} (top) or S^{2-}/S^{-}(bottom) species during cycling species as deduced from XPS analysis (b) Evolution of Fe^{3+}/Fe^{2+} species during cycling species as deduced from Mössbauer spectra analysis.

The Mössbauer spectrum of the pristine compound can be interpolated using four doublets revealing a complex distribution of high and low spin Fe^{2+} as already observed for LTFS (cf. figure S14).[6] All along

the charge plateau, the Fe^{2+} components decrease in intensity in favor of the Fe^{3+} ones (cf. figure 6b). Reversibly in discharge, the Fe^{3+} components progressively decrease in intensity and the spectrum observed at the end of the discharge is comparable to that of pristine. If we now consider the degree of oxidation of niobium, the XPS data (cf. figure 6a top) indicate that the pristine material is composed mainly of Nb^{5+}. During charge, the Nb^{5+} component decreases at the expense of Nb^{4+}. At the contrary, the Nb^{5+}/Nb^{4+} ratio increases through discharge without reaching the value observed in the pristine phase. It is important to note that the oxidation of iron in charge cannot explain the charge compensation fully, especially considering the competitive reduction of niobium. It is then necessary to consider the charge of sulfur. The XPS data (cf. figure 6a bottom) indicate that in the pristine phase, the sulfur is mostly in the S^{2-} form with a minority S^{n-}(oxidized sulfur) component. During the charge, this oxidized component increases at the expense of S^{2-} and then decreases again during the discharge, without however fully returning to the pristine structure. Thus, the lithium withdrawal in LNFS is compensated by the simultaneous oxidation of iron and sulfur. However, this compound differs from the structurally close compound $Li_{1.13}Fe_{0.3}Ti_{0.4}S_2$, where the oxidation of sulfur follows that of iron at least at the first charge.[6] This could explain the observed single plateau for LNFS in contrary to the initial sloppy voltage profile followed by plateau region for LTFS. Moreover, like the Li_3NbS_4 compounds, the reduction of niobium in charge suggests a reductive coupling mechanism between sulfur and niobium without however involving the second cation present, namely iron. In short, Fe^{2+} substitution in Li_3NbS_4 leads to a Li-rich layered structure showing anionic redox activity alike few other Li-rich Fe substituted compounds in the literature.[19]

6. Discussion

Through this work we have highlighted two ways to activate the anionic redox in Li_3NbS_4, namely by disordering the cationic network or by substituting Nb with Fe. It is now important to rationalize these findings through more theoretical considerations. First-principles DFT calculations were performed on the two Li_3NbS_4 polymorphs using the VASP program package (see Supplementary information for details). The calculation results show that the ordered polymorph is more stable than the disordered one, by at least 400 meV/FU. Both polymorphs display quite different electronic structures (cf. figure 7). The ordered phase exhibits the typical electronic band features of a molecular solid with a significant band gap and weakly dispersive bands. The electronic structure computed for an isolated $Li_{12}Nb_4S_{16}$ cluster (Figure S15) in a 10x10x10 $Å^3$ simulation box resembles that of the ordered phase with a greater discretization of the bands consistent with the absence of inter-cluster interactions. According to the Bloch theory, such a one-to-one correspondence between the molecular states of the $Li_{12}Nb_4S_{12}$ cluster and the band structure of the ordered phase demonstrates that the

latter is made of weakly interacting clusters that can therefore be considered as electronically isolated from each other in the condensed phase. The fukui functions computed both for the isolated cluster and ordered phase reveal that the external S^{2-} sulfides located at the periphery of the Nb_4S_{16} cluster will be primarily involved in the oxidation process through their lone-pairs pointing towards the Li^+ ions. Both the strongly localized character of these electronic states and the absence of inter-cluster covalent interactions are then consistent with the absence of electrochemical activity of the o-Li_3NbS_4 phase. In contrast, the electronic structure of the disordered polymorph shows quite dispersive bands and a small band gap, indicative of significant inter-cluster covalent interactions. Among the various Li/Nb distributions investigated in this study to account for the disorder, the structure having a large number of Nb-S-Nb connections are far most stable than the ones leaving some sulfur atoms uncoordinated to any Nb metal. Moreover, all relaxed structures show quite distorted Nb-environments with 4, 5 or 6 surrounding S^{2-} anions, consistent with the absence of crystal field stabilization for the Nb^{5+} cations. Such structural and electronic features contribute to the enhancement of Nb(d)-S(p) orbital mixing through the lowering of the local symmetry and to the opening of an electron-delocalization pathway which both favor the activation of the electrochemical activity of d-Li_3NbS_4. This result confirms our recent report stating that the difficulty encountered in triggering the anionic redox activity in Li_2TiS_3 was nested in the "isolation" of electrons at the Fermi level that are mainly localized in non-bonding S(p) orbitals in presence of d^0 transition metal cations.[7] We could escape from this trap by enhancing hybridization via a distortion of the MX_6 octahedra by partial substitution of S by Se. Comforting this analogy, anionic redox activity could also be triggered in Li_2TiS_3 by increasing disorder via ball milling. Disorder acts as a lever to lower the symmetry of the sulfur sites therefore increasing the number of sulfur p-orbitals that can interact (hybridize) with the metal d-orbitals and opening electron-delocalization paths for activating anionic redox in d^0 metal compounds.

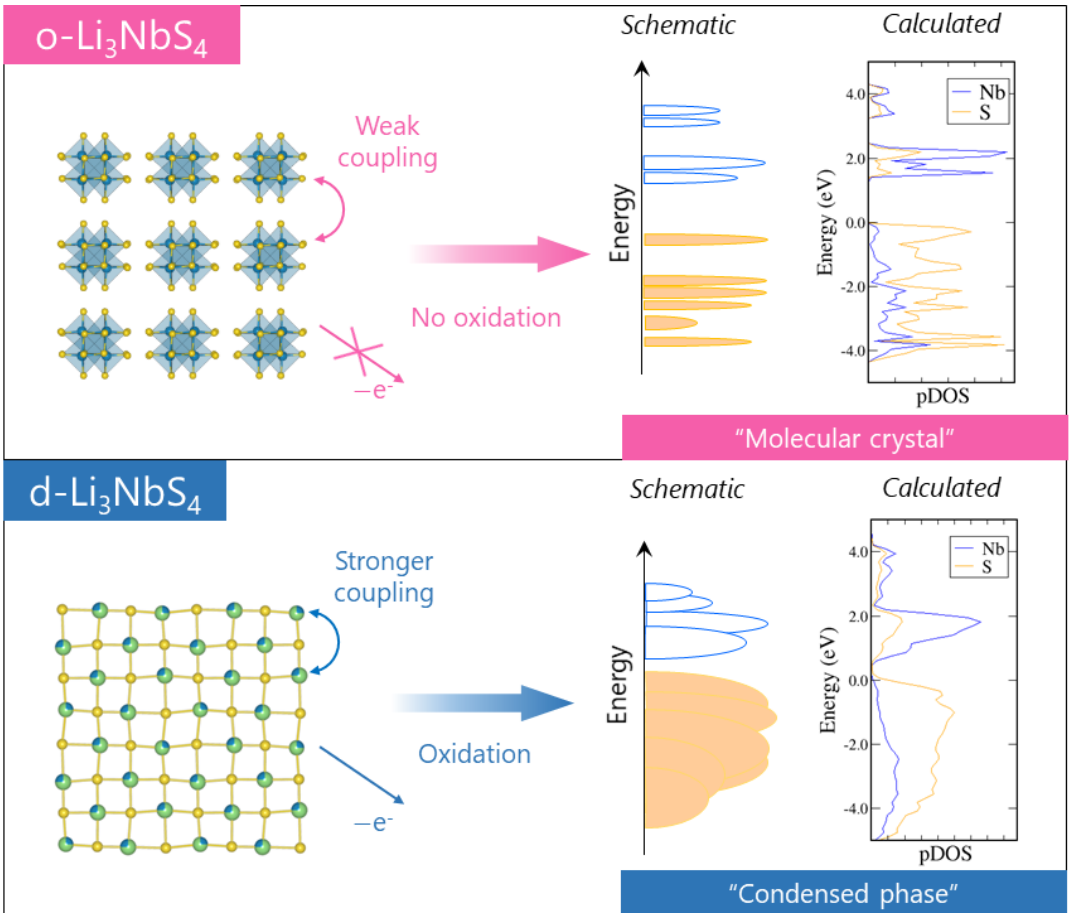

Figure 7: Comparison of the electronic structures of o-Li_3NbS_4 and d-Li_3NbS_4. The weak coupling between the Nb_4S_{16} clusters leads to a band structure close to a molecular crystal. On the contrary, cationic disorder in d-Li_3NbS_4 enhances the number of NbS_x connections and Nb(d)-S(p) hybridization which increases the band width and decreases the band gap of its electronic structure, therefore opening electron delocalization paths. . The DOS represented on the right have been obtained by DFT.

It is now important to ask, what is the best synthesis strategy to optimize the performances of d^0-based Li_2MX_3 compounds? An obvious advantage of the disorder approach resides in the activation of the electrochemistry without modifying the chemical composition of the compound and thus without modifying its capacity. On the contrary, cationic or anionic substitution reduces the theoretical capacity of the material (for instance the theoretical capacity of LNFS is 244 $mAh.g^{-1}$ vs 332 $mAh.g^{-1}$ for Li_3NbS_4). However, disordered materials show limited capacity retention limits on long term cycling due to hazardous lithium percolation paths or more likely due to copious parasitic reactions taking place at the surface of this highly divided material. However, such drawbacks partially vanish by using them in solid state batteries while coupling with suitable solid state electrolyte, as demonstrated by Sakuda et al.[9] With further understanding of the materials bulk and surface properties, it is possible to

fully exploit the beneficial aspects of these Li-rich disordered sulfide phases could have for the next generation of solid state Li-ion batteries.

To conclude, we have synthesized by a ceramic way a new Li_3NbS_4 polymorph isostructural to Li_3NbO_4. Surprisingly this compound does not show any electrochemical activity in oxidation contrary to the disordered polymorph obtained by mechanosynthesis. The origin of this difference in performance was initially associated with two parameters, namely the particle size and/or the degree of cationic disorder. By inducing cationic disorder in the ordered polymorph via electrochemical reduction (i.e. without modifying the particle size) we could establish a direct link between cationic disorder and the possibility to oxidize the compound. XPS studies of the charge compensation mechanisms demonstrated that the oxidation of Li_3NbS_4 polymorphs proceeds by an anionic sulfur redox mechanism. Moreover, from DFT analysis the difference in electrochemical activity between the two polymorphs could be rationalized. Indeed, the disorder induces a hybridization of the electronic levels at the Fermi level which enhances electronic delocalization in the structure, therefore triggering electrochemical activity. Finally, we have also shown the possibility of activating the anionic redox of Li_3NbS_4 by realizing a Li_3NbS_4/FeS solid solution. Although anionic redox processes have been widely studied in disordered rocksalt compounds, this study enables for the first time to our knowledge, to spot the influence of cationic disorder in a d^0 compound whose activity is solely triggered by a purely anionic electrochemical process. The feasibility to activate anionic redox via disorder comfort early results and offers a new wide design space to solid state chemists for preparing new high capacity Li-rich sulfide compounds that are high coveted for making solid state batteries based on sulfide-based electrolytes as well.

Acknowledgements

Use of the 11-BM mail service of the APS at Argonne National Laboratory was supported by the US Department of Energy under contract No. DE-AC02-06CH11357 and is gratefully acknowledged. ALBA experiments were performed through academic proposal 2020024152 and François Fauth is acknowledged for his kind help for the measurement on MSPD beamline. Access to TEM facilities was granted by the Advance Imaging Core Facility of Skoltech. T.M. acknowledges the Ecole Normale Supérieure Paris-Saclay for his PhD scholarship and J.-M.T. acknowledges the funding from European Research Council (ERC) (FP/2014)/ERC grant/project no.670116-ARPEMA.

Conflict of interest

The authors declare no conflict of interest.

Associated Content

*Supporting Information

The Supporting Information containing additional XRD and electron diffraction patterns, crystallographic details, further XPS and Mossbauer data and electrochemical analyses is available free of charge on the ACS Publications website.

References

(1) Armand, M.; Tarascon, J.-M. Building Better Batteries. *Nature* **2008**, *451* (7179), 652–657. https://doi.org/10.1038/451652a.

(2) Lu, Z.; Dahn, J. R. Understanding the Anomalous Capacity of Li/Li[NixLi(1/3−2x/3)Mn(2/3−x/3)]O2 Cells Using In Situ X-Ray Diffraction and Electrochemical Studies. *J. Electrochem. Soc.* **2002**, *149* (7), A815. https://doi.org/10.1149/1.1480014.

(3) Assat, G.; Tarascon, J. M. Fundamental Understanding and Practical Challenges of Anionic Redox Activity in Li-Ion Batteries. *Nat. Energy* **2018**, *3* (5), 373–386. https://doi.org/10.1038/s41560-018-0097-0.

(4) Seo, D. H.; Lee, J.; Urban, A.; Malik, R.; Kang, S.; Ceder, G. The Structural and Chemical Origin of the Oxygen Redox Activity in Layered and Cation-Disordered Li-Excess Cathode Materials. *Nat. Chem.* **2016**, *8* (7), 692–697. https://doi.org/10.1038/nchem.2524.

(5) Sathiya, M.; Abakumov, A. M.; Foix, D.; Rousse, G.; Ramesha, K.; Saubanère, M.; Doublet, M. L.; Vezin, H.; Laisa, C. P.; Prakash, A. S.; Gonbeau, D.; Vantendeloo, G.; Tarascon, J. M. Origin of Voltage Decay in High-Capacity Layered Oxide Electrodes. *Nat. Mater.* **2015**, *14* (2), 230–238. https://doi.org/10.1038/nmat4137.

(6) Saha, S.; Assat, G.; Sougrati, M. T.; Foix, D.; Li, H.; Vergnet, J.; Turi, S.; Ha, Y.; Yang, W.; Cabana, J.; Rousse, G.; Abakumov, A. M.; Tarascon, J. M. Exploring the Bottlenecks of Anionic Redox in Li-Rich Layered Sulfides. *Nat. Energy* **2019**, *4* (11), 977–987. https://doi.org/10.1038/s41560-019-0493-0.

(7) Leube, B. T.; Robert, C.; Foix, D.; Porcheron, B.; Dedryvère, R.; Rousse, G.; Salager, E.; Cabelguen, P.-E.; Abakumov, A. M.; Vezin, H.; Doublet, M.-L.; Tarascon, J.-M. Activation of Anionic Redox in D0 Transition Metal Chalcogenides by Anion Doping. *Nat. Commun.* **2021**, *12* (1), 5485. https://doi.org/10.1038/s41467-021-25760-8.

(8) Sakuda, A.; Takeuchi, T.; Kobayashi, H.; Sakaebe, H.; Tatsumi, K.; Ogumi, Z. Preparation of Novel Electrode Materials Based on Lithium Niobium Sulfides. *Electrochemistry* **2014**, *82* (10), 880–

883. https://doi.org/10.5796/electrochemistry.82.880.

(9) Sakuda, A.; Takeuchi, T.; Okamura, K.; Kobayashi, H.; Sakaebe, H.; Tatsumi, K.; Ogumi, Z. Rock-Salt-Type Lithium Metal Sulphides as Novel Positive-Electrode Materials. *Sci. Rep.* **2014**, *4*, 2–6. https://doi.org/10.1038/srep04883.

(10) Fauth, F.; Boer, R.; Gil-Ortiz, F.; Popescu, C.; Vallcorba, O.; Peral, I.; Fullà, D.; Benach, J.; Juanhuix, J. The Crystallography Stations at the Alba Synchrotron. *Eur. Phys. J. Plus* **2015**, *130* (8). https://doi.org/10.1140/epjp/i2015-15160-y.

(11) Fauth, F.; Peral, I.; Popescu, C.; Knapp, M. The New Material Science Powder Diffraction Beamline at ALBA Synchrotron. *Powder Diffr.* **2013**, *28* (S2), S360–S370. https://doi.org/10.1017/S0885715613000900.

(12) Rodríguez-Carvajal, J. Recent Advances in Magnetic Structure Determination by Neutron Powder Diffraction. *Phys. B Phys. Condens. Matter* **1993**, *192* (1–2), 55–69. https://doi.org/10.1016/0921-4526(93)90108-I.

(13) Chamas, M.; Sougrati, M. T.; Reibel, C.; Lippens, P. E. Quantitative Analysis of the Initial Restructuring Step of Nanostructured FeSn2-Based Anodes for Li-Ion Batteries. *Chem. Mater.* **2013**, *25* (12), 2410–2420. https://doi.org/10.1021/cm400253a.

(14) Ukei, K.; Suzuki, H.; Shishido, T.; Fukuda, T. Li3NbO4. *Acta Crystallogr. Sect. C Cryst. Struct. Commun.* **1994**, *50* (5), 655–656. https://doi.org/10.1107/s010827019300890x.

(15) Jacquet, Q.; Perez, A.; Batuk, D.; Van Tendeloo, G.; Rousse, G.; Tarascon, J. M. The Li3RuyNb1-YO4 (0 ≤y ≤1) System: Structural Diversity and Li Insertion and Extraction Capabilities. *Chem. Mater.* **2017**, *29* (12), 5331–5343. https://doi.org/10.1021/acs.chemmater.7b01511.

(16) Drezen, T.; Kwon, N. H.; Bowen, P.; Teerlinck, I.; Isono, M.; Exnar, I. Effect of Particle Size on LiMnPO4 Cathodes. *J. Power Sources* **2007**, *174* (2), 949–953. https://doi.org/10.1016/j.jpowsour.2007.06.203.

(17) Sathiya, M.; Rousse, G.; Ramesha, K.; Laisa, C. P.; Vezin, H.; Sougrati, M. T.; Doublet, M. L.; Foix, D.; Gonbeau, D.; Walker, W.; Prakash, A. S.; Ben Hassine, M.; Dupont, L.; Tarascon, J. M. Reversible Anionic Redox Chemistry in High-Capacity Layered-Oxide Electrodes. *Nat. Mater.* **2013**, *12* (9), 827–835. https://doi.org/10.1038/nmat3699.

(18) Casimir, H. B. G.; Wang, Z.; Fan, S.; Yu, Z.; Fan, S.; Kamal, A.; Clarke, J.; Devoret, M. H.; Kodera, T.; Sounas, D. L.; Caloz, C.; Kang, M. S.; Butsch, A.; Russell, P. S. J.; Lira, H.; Yu, Z.; Fan, S.; Lipson, M.; Sounas, D. L.; Caloz, C.; Lepri, S.; Casati, G.; Luo, C.; Joannopoulos, J. D.; Fan, S.; Shadrivov, I. V; Fedotov, V. A.; Powell, D. A.; Kivshar, Y. S.; Zheludev, N. I.; Yuan, B.; Cheng, J. C.; Guo, X. S.; Tu, J.; Zhang, D.; Cheng, J. C.; Theocharis, G.; Daraio, C.; Zou, X.; Liang, B.; Cheng, J.; Zhang, S.; Shui, X.; Kaya, O. A.; Ulug, B.; Kim, H. W.; Seung, H. M. Unlocking the Potential of Cation-Disordered Oxides for Rechargeable Lithium Batteries. *Science (80-.).* **2014**, *343* (January), 519–

523.

(19) Yabuuchi, N.; Takeuchi, M.; Nakayama, M.; Shiiba, H.; Ogawa, M.; Nakayama, K.; Ohta, T.; Endo, D.; Ozaki, T.; Inamasu, T.; Sato, K.; Komaba, S. High-Capacity Electrode Materials for Rechargeable Lithium Batteries: Li3NbO4-Based System with Cation-Disordered Rocksalt Structure. *Proc. Natl. Acad. Sci. U. S. A.* **2015**, *112* (25), 7650–7655. https://doi.org/10.1073/pnas.1504901112.